Article

Morphological changes of the south-eastern wall of Askja caldera, Iceland over the past 80 years

Check for updates

Alina V. Shevchenko [1] ✉, Thomas R. Walter [1], Magnus T. Gudmundsson [2], Joaquín M. C. Belart [3], Pouria Marzban [1,4], Edgar U. Zorn [5], Þorsteinn Sæmundsson[2], Jón Kristinn Helgason[6], Jens M. Turowski[1], Magdalena S. Vassileva [1,7], Mahdi Motagh[1,7] & Daniel Müller[1]

Calderas are subcircular depressions with near-vertical walls, which are often gravitationally unstable and prone to mass movements that sequentially widen their basins. However, the details of these erosional changes are difficult to decipher due to short observational periods. Here, we use a photogrammetric dataset of nearly 80 years to study the landslide-prone south-eastern wall of Askja caldera (Iceland). We analyzed aerial data from 1945 and 1987, stereo satellite data from 2013 and 2022, and drone images acquired in 2019, 2022, and 2023. We developed an inventory of geomorphological features and identified types of slope instability. We describe over 700 features, including circa 500 fractures, 200 sinkholes, and four major landslides. We found that morphological changes were persistent over the observation period, accumulating in a sector that collapsed in 2014. We discuss various factors of slope instability at Askja including possible volcano-permafrost interaction, and other processes that could induce mass wasting.

Large eruptions and mass wasting at volcanoes can produce extensive negative relief landforms, such as amphitheaters following sector collapse[1] or calderas in case of collapse of a magma chamber[2]. So far scientific interest has focused mainly on large volcanic collapses[3,4], which can trigger tsunamis and explosions with an impact at greater distances[5]. However, smaller-scale mass movements can also pose a great danger and are more likely to occur[6]. These are syn- or post-eruptive rockfalls, partial lateral collapses, and landslides that can occur on steep volcanic slopes or caldera walls and cause cascading events such as lahars or tsunamis.

Volcanic slope instability is caused by various processes, such as eruptive and tectonic deformation, earthquakes, over-steepening, and peripheral erosion[7]. In addition, mechanical weakening, including hydrothermal alteration or permafrost thawing, could play a big role in initiating volcanic slope instability[8]. However, the specific processes of volcano-cryosphere interaction are poorly understood, and the hazards associated with the instability of volcanic slopes in permafrost regions are unclear.

Flank instability associated with caldera structures may evolve during different phases of caldera evolution, such as during caldera collapse forming megabreccias inside the caldera basin[9] or during later erosional stages that occur on the inside[10], and on the outside[11] of caldera faults.

Landslides occurring inwardly are especially common, and may particularly cluster shortly after caldera formation. As an example, the Mijakejima caldera formed in 2000[12] and widened within weeks after its formation from 900 m to 1600 m[13] due to inward collapses and rock falls[14].

In this study, we focus on the inward-facing slope instability at the south-eastern (SE) Askja caldera wall, which combines several complexities, such as steep morphology, recent formation (1875), and hydrothermal activity. Moreover, this volcano is located in a high-latitude and high-altitude region, which makes it a natural laboratory for studying volcano-cryosphere interaction, and its effects on slope stability.

Askja is part of the Dyngjufjöll volcanic complex located in Iceland's North Volcanic Zone about 30 km north of the Vatnajökull ice cap and consists of at least three calderas (Kollur, Askja, and Öskjuvatn)[15–17]. In 1875, Askja (Fig. 1) was the source of a large Plinian eruption that formed Öskjuvatn caldera subsequently filled by water forming a lake. These two calderas, Askja and Öskjuvatn, overlap and therefore for simplicity together are referred to as Askja caldera. After a period of quiescence, seven small-volume eruptions occurred in the 1920s along the new Öskjuvatn caldera ring faults and on the southern outer slope[18]. The most recent eruption occurred in 1961 on the northern side of Öskjuvatn[19]. Askja experienced

[1]GFZ German Research Centre for Geosciences, Potsdam, Germany. [2]Institute of Earth Sciences, University of Iceland, Reykjavík, Iceland. [3]National Land Survey of Iceland, Akranes, Iceland. [4]German Archaeological Institute (DAI), Berlin, Germany. [5]Ludwig-Maximilians-Universität München, Munich, Germany. [6]Icelandic Meteorological Office, Reykjavík, Iceland. [7]Institute of Photogrammetry and GeoInformation, Leibniz University Hannover, Hannover, Germany. ✉e-mail: alinash@gfz-potsdam.de

Fig. 1 | The study site. a Hillshade map of Askja caldera based on the 2016 ÍslandsDEM by the National Land Survey of Iceland (LMI) (https://dem.lmi.is) with the main eruptive features indicated. The dotted rectangle outlines the study area. The inset shows the position of Askja in Iceland within the North Volcanic Zone. **b** Oblique visualization of the study area rendered from the virtual 3D space based on the 2022 Plèiades data (https://cnes.fr/projets/Plèiades). The main post-1875 vent and fissure locations are based on the previous study[17].
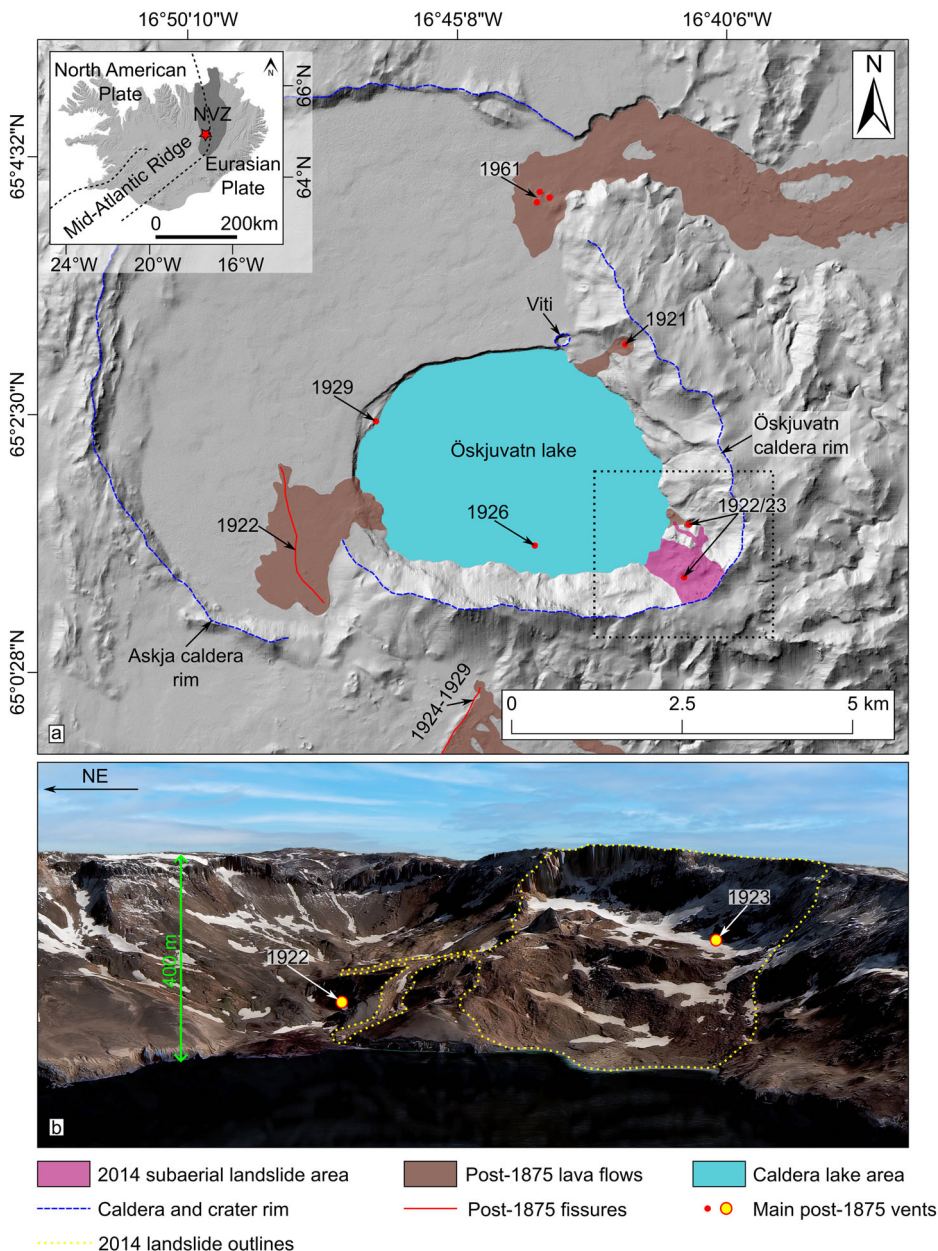
long periods of subsidence interrupted by short periods of uplift. Geodetic measurements began in 1966 and showed rapid inflation in the early 1970s of 20 cm per year[20], reversing to slow subsidence in the late 1970s, which increased to 6-10 cm per year until 1987[20,21], and decreased in the following decades to <5 cm per year[22]. In 2021, another episode of rapid uplift started[23] locally exceeding 70 cm per year[24].

On 21.07.2014, a large landslide occurred at the SE Askja caldera wall, which resulted in large morphological changes and caused a tsunami in the Öskjuvatn lake[25–27]. Elíasson and Sæmundsson[28] studied the landslide morphology via comparison of the pre- and post-landslide digital elevation models (DEMs), estimated the volume to be 20×10^6 m³, and described the landslide movement as rotational in a slip circle. The triggering factors of this landslide discussed in previous studies are precipitation, seismic activity, and hydrothermal weakening[27,29]. Besides, it is currently subject to intense debate if the widespread slope movements in Iceland, including at Askja, are enhanced by the retreat of permafrost[23,30,31].

Askja has been studied with different remote sensing techniques. Due to the frequent cloud cover and dark winter periods, recent studies relied on satellite synthetic aperture radar (SAR) data[22–24]. However, SAR techniques

are not entirely reliable in steep slope analysis due to geometric distortion[32]. Therefore, here we use photogrammetric analysis of the nearly 80-year high-resolution optical dataset[33] (Supplementary Fig. 1). The photogrammetric data reveals the morphological features and changes occurring at the steep walls of Askja even before the Interferometric SAR and Global Navigation Satellite System eras, which let us investigate the possible link between different processes acting towards flank instability.

Results

The archive photogrammetric datasets from 1945 and 1987, the stereo satellite datasets from 2013 and 2022, and the repeated visible and infrared drone data from 2019, 2022, and 2023 provide a 78-year-long incremental view of the morphological changes on the SE wall of Askja caldera (Supplementary Fig. 2), as well as the recent apparent ground surface temperatures. In particular, we can identify the rim of the caldera, the steep slopes, and the outline of Öskuvatn Lake in all datasets, thus allowing the detection of material removal and accumulation, as well as local features relevant to understanding the morphodynamics at the study area. Below we first provide a detailed morphological analysis of the observed features, then
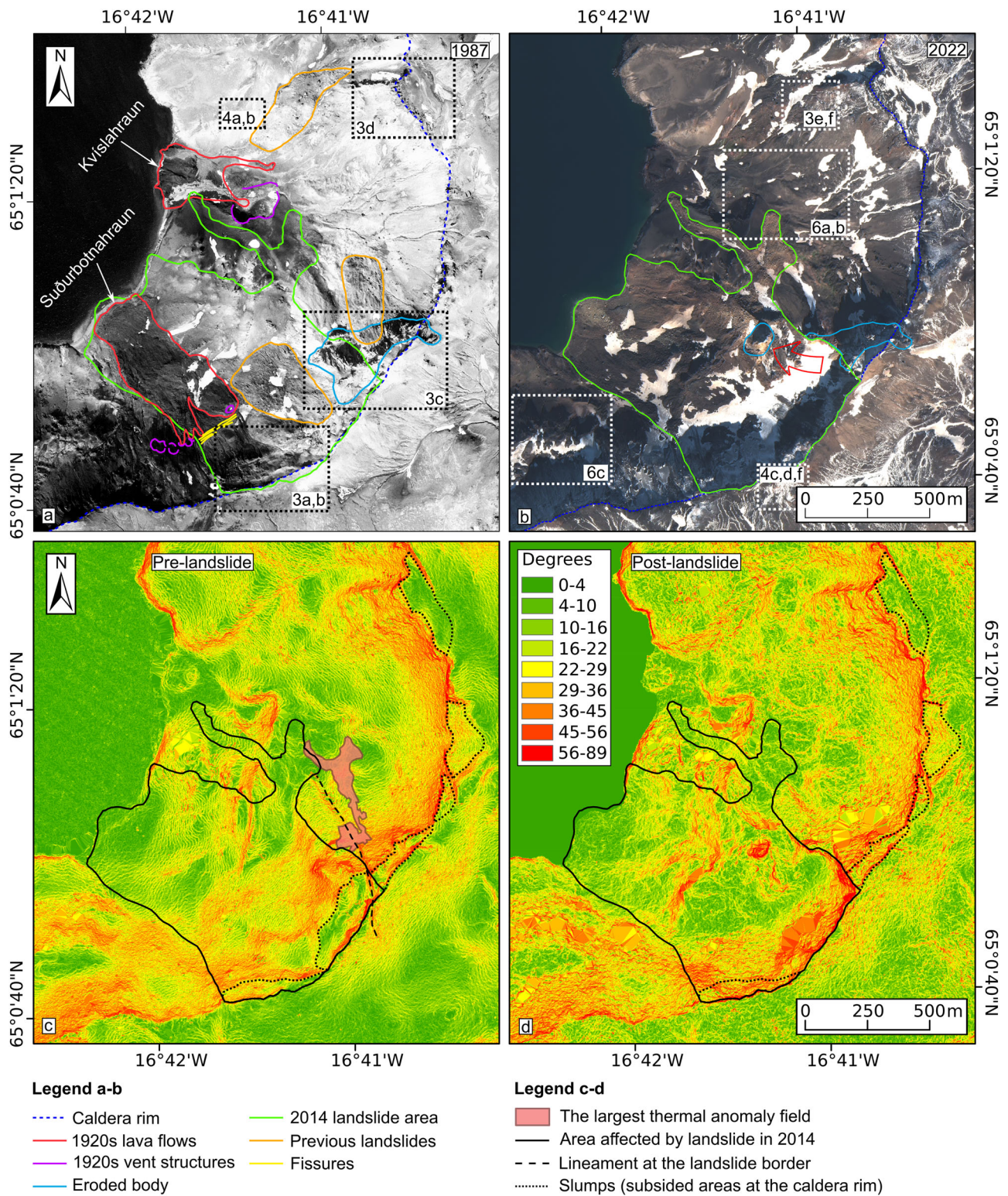
Fig. 2 | Morphological features of the SE caldera wall. a The orthophoto generated from 1987 aerial data (www.lmi.is). **b** The orthophoto generated from 2022 Plèiades data. The red arrow shows the supposed sliding direction of the intact block (obelisk). **c, d** Slope maps. Dotted rectangles outline the areas shown in Figs. 3, 4, and 6.

we present the results of the 2D mapping, and finally the results of 3D analysis and the volumetric changes.

Morphological analysis

The photogrammetric archives (1945 and 1987) show several eruptive features from the 1920s activity (Fig. 2a shows the 1987 orthophoto since it has better quality than the 1945 orthophoto). There are outlines of two lava

flows (northern - Kvíslahraun, origin. Dec. 1922, and southern—Suður-botnahraun, origin. Feb. 1923). The major part of the southern lava flow was covered by the landslide masses in 2014. Circular and semi-circular features adjacent to the southern lava flow can be interpreted as vents or explosion craters (Supplementary Fig. 3a). Three of them have visible signs of lava outpouring. The area also presents several fissures likely associated with the eruption. The south-western (SW) border (levee) of the southern lava flow

seen in the archive images partially matches the SW flank of the later 2014 landslide. This implies that landslide morphology was already pronounced decades before the failure, inhibiting the southern lava flow and overlaying its surface. We find that the northern lava flow area has two vents; one is located on the slope above, while the second vent is located inside an open crater, which is surrounded by cinder material (Supplementary Fig. 3b).

In the upper eastern area of the caldera wall that was later affected by the 2014 landslide, a strongly eroded body, which is cut through with about 20 erosional chutes, can be observed, the eastern part of which continues into the caldera's outer slope (Fig. 2a, Fig. 3c, Supplementary Fig. 4b). The body was bisected during the 2014 landslide; a part of it slid down and may have been deposited as an intact block resembling an obelisk, now located lower on the slope of the caldera wall (Fig. 2b). We distinguish three landslide deposits by the coarse material of their surfaces different from the adjacent areas of the caldera wall (Fig. 2a, Supplementary Fig. 4). These landslides were emplaced before 1945, as they are already evident in the 1945 images. One was located in the area later covered by the 2014 landslide. The second is located close to the north-eastern (NE) flank of the 2014 landslide and most likely emerged from the gradual sliding of parts of the material from the eroded body. The third landslide is located in the northern part of the study area with a crown visible at the caldera rim.

The slope maps generated from the 2013 and 2022 Plèiades DEMs allow us to explore the 2014 landslide and other topographic changes in detail. Figure 2c, d reveals the subsided areas adjacent to the caldera rim with a height reduction of up to 20 m. These areas resemble slumps since they represent a short-distance mass wasting of a coherent material. A part of one of the slumps (the eroded body described above) had been undergoing noticeable changes since 1945 and collapsed during the 2014 landslide (Figs. 2c, d and 3g). Thus, we can assume that other areas showing topographic losses visible at the caldera rim should be considered unstable, which matches the observation reported in previous studies[34,35]. We can also observe an NNW-SSE lineament that cuts the eroded body and the outer and inner slopes of the caldera, partially matches the later 2014 landslide flank and is aligned with the trend of the largest thermal anomaly field (Fig. 2c).

Numerous fractures and sinkholes can be identified in the 1945 orthophoto and the new ones that emerged after 1945 can be observed in the 1987, 2019, 2022, and 2023 orthophotos. The 2013 dataset has extensive snow cover and thus it has not been used for the feature analysis (see Supplementary Discussion).

In the photogrammetric archives (1945 and 1987), we found a long fracture following the upper rim at a 30 m distance (Fig. 3a). The fracture casts a shadow; thus, it likely has an opening (tensile) component. The 1987 DEM shows that this fracture has a vertical offset of up to 3 m in its western part. Comparison to the later dataset of 2022 reveals that this fracture was reactivated during the 2014 landslide, as it partially matches the 2014 landslide crown (Fig. 3b). Therefore, we can consider such tensile fractures as morphological precursors of potential landslides showing their locations.

The fractures have been mainly developing at the caldera outer slopes adjacent to the rim. We observe a slump outlined by tensile fractures (Fig. 3d). It has a vertical offset of about 20 m relative to the caldera rim (Fig. 3h) and is of unknown age. A 10 m horizontal displacement of this slump, which occurred between 1987 and 2013, is visible in the profiles (Fig. 3h). Below this slump, numerous newly emerged fractures and open cracks are visible via the comparison of the 1987 and 2022 orthophotos (Fig. 3e, f). Some features like rock fragments are displaced downslope, which could imply ongoing creep. Figure 3c and profile (Fig. 3g) represent a similar but more developed slump (the eroded body discussed above), which had undergone about 15 m vertical and 5 m horizontal displacement since 1987 before partially collapsing during the 2014 event.

The newly emerged features can be identified within the study area throughout the dataset. Figure 4b shows an open crack that developed after 1987 (not visible in the 1945 and 1987 orthophotos (Fig. 4a)) in the area to the north of the 2014 landslide, which also demonstrates patterns of rock alteration.

Multiple new sinkholes can be observed, some of them were identified within the 2014 landslide deposits (Supplementary Fig. 5a). Our long-term dataset allows us to analyze the development of a relatively large sinkhole (Fig. 4c–f) that emerged after 1945 in the area adjacent to the later 2014 landslide crown. In 1987, the sinkhole area was 130 m², and in 2023, it became 232 m². The topographic profiles show that the sinkhole depth was 3 m in 2022 and 5 m in 2023, which can also depend on the amount of snow in the sinkhole. This sinkhole, the largest sinkhole detected (or explosion crater; Supplementary Fig. 5c), and the row of craters and vents from the 1923 eruption are aligned NWW-SEE and thus possibly associated with a pronounced fracture system. Some of the sinkholes developed at fractures visible adjacent to the caldera rim (Supplementary Fig. 5b). Therefore, the sinkholes, although not directly related to slope instability, may indirectly allow the identification of structures relevant to unstable flanks.

The visible and infrared drone data acquired since 2019 let us investigate the fumarolic field and several thermal anomalies located adjacent to the 2014 landslide area (Fig. 5). According to our data, the highest apparent surface temperature of the fumarolic field is about 60 °C. Although these temperatures are path and dimension affected and thus need to be treated with caution (see Supplementary Discussion), this is the largest thermal anomaly field located in the study area—about 22,000 m². A fracture is visible within the field, from which the fumarolic steaming occurs, indicating that degassing and hydrothermal activity is fracture controlled.

We distinguish four areas of a rugged surface indicative of underground material transfer and ground motion. One such area (Fig. 6a, b) is located in the middle of the SW caldera wall above the open crater of the 1922 (Kvíslahraun) eruption. The surface of this area is presented by numerous longitudinal (along the slope) and compressional (perpendicular to the slope) ridges with elliptical depressions between them, which is similar to surfaces of inactive or relict rock glaciers (see Discussion section). A large thermal anomaly associated with the fumarolic field described above is located 130 m south of this rugged surface. Another rugged terrain is characterized by near-rectangular polygons (about 30 m in map view) in its central part (Fig. 6c, d), which bears similarities with ice-wedged polygon patterned ground (see Discussion section). It is located in the southern part of the study area and contains the largest observed sinkhole or explosion crater (Supplementary Fig. 5c); several thermal anomalies are located close to the NE part of this terrain, implying a possible association of the morphological features to geothermal activity.

2D mapping

We used the photogrammetric dataset to map the main structural and morphological features and develop a geomorphologic inventory associated with slope instability in the SE Askja caldera wall (Fig. 7). Eruptive features include two lava flows and five effusive vents associated with the 1922–1923 unrest. Fumarolic vents located at the upper part of the 2014 landslide (Supplementary Fig. 6), several explosion craters (some of which lack a deposition aureole and therefore could also be large sinkholes), and multiple thermal anomalies were mapped.

Several areas prone to future landslides were outlined based on the interpretation of our multitemporal dataset and material published before[34,35]. These areas include slumps at the caldera rim and adjacent parts of the caldera wall. Some of them have high fracture density and/or demonstrate slope movements. The largest unstable area at the caldera rim is 225,000 m² in map view and includes one of the largest slumps and a creeping sector of the slope located below it (Fig. 3f). It has also the highest concentration of fractures (up to 90 per 1 km²) and has shown horizontal displacement since 1945 (Fig. 3h).

The inventory contains a total of 525 fractures, among which 81 are noticeable in the 1945 dataset, 36 appeared from 1945 to 1987, 122 appeared between 1987 and 2019, 263 emerged during 2019–2022, and 23 appeared in 2022–2023 in the areas captured by the limited extent drone survey (see Supplementary Discussion).
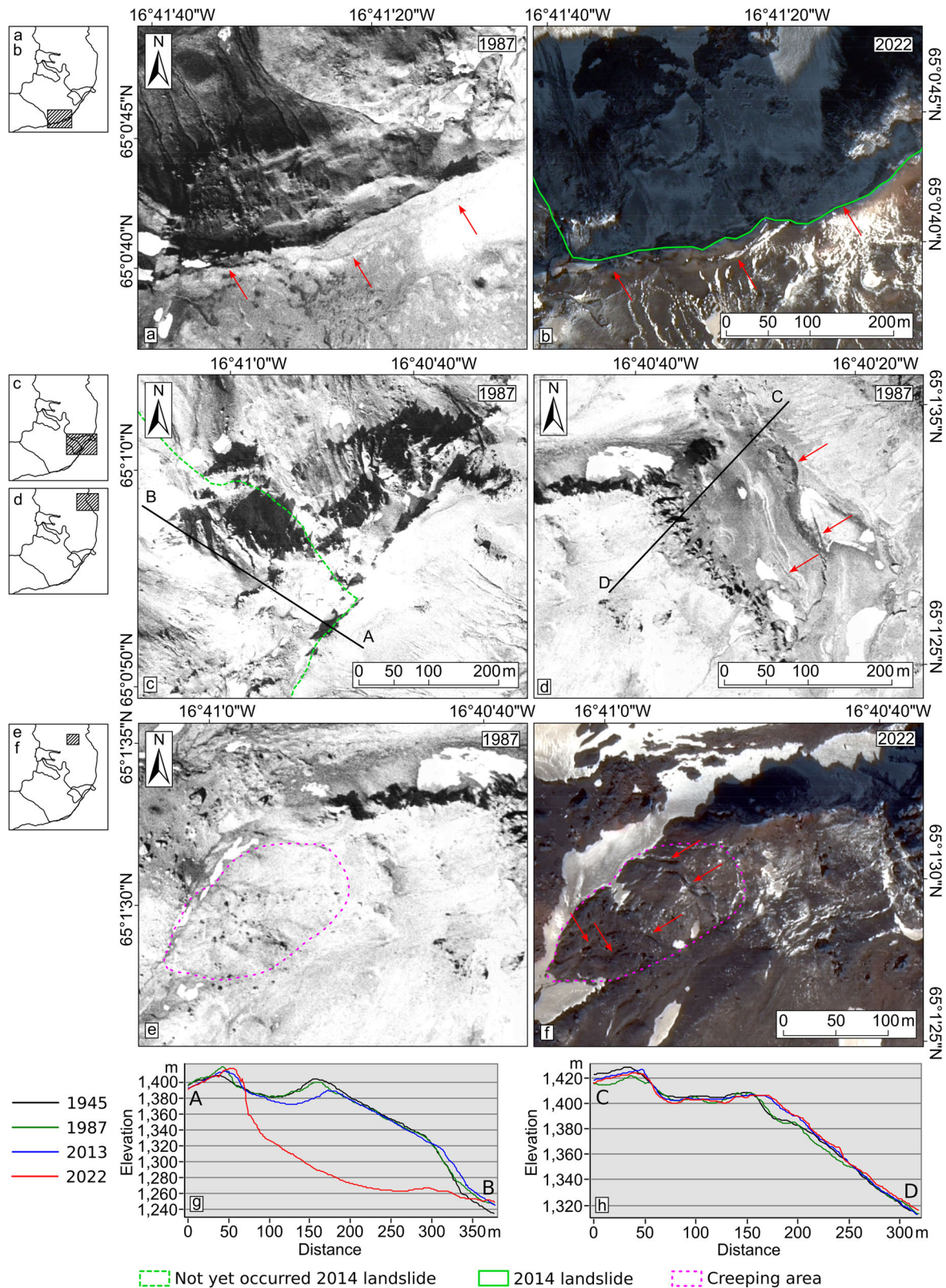
Fig. 3 | Slope instability features at the SE caldera wall. a Area of the later 2014 landslide crown shows tensile fracture emerging decades before the landslide. **b** The 2014 landslide crown partially matches the previously developed fracture. **c, d** Slumps developed at the caldera rim. One (**c**) at the later 2014 landslide area. **e, f** Fractures and open cracks developed since 1987 in the area below the slump (**d**), which could imply a creep-like motion. **g, h** Profiles taken through 1945, 1987 archive and 2013, 2022 Plèiades DEMs; the profile lines are shown in (**c, d**). Fractures are shown with red arrows. **a, c–e** 1987 archive orthophoto; **b, f** 2022 Plèiades orthophoto. Insets on the left show the locations of the subfigures as hatching rectangles within the study area.
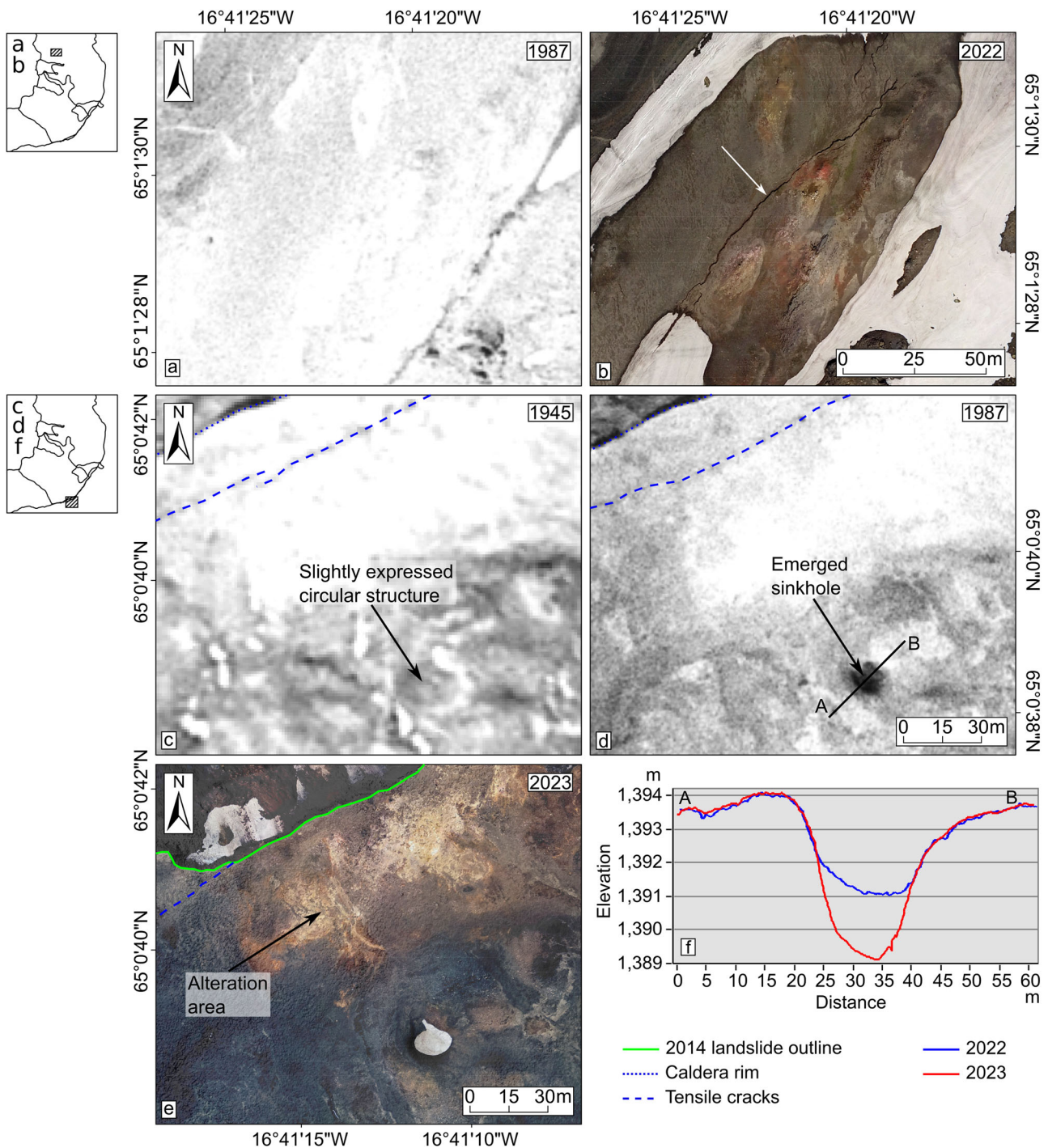
Fig. 4 | New emerging fractures and sinkholes. a, **b** Area to the north from the 2014 landslide shown in the 1987 archive and 2022 drone orthophotos. An open fracture that developed after 1987 is pointed to with a white arrow. **c–e** Area adjacent to the 2014 landslide crown shown in 1945 and 1987 orthophotos, and in 2023 textured DEM presenting the development of a new sinkhole. **f** The profile through the sinkhole taken from the 2022 and 2023 drone DEMs. Insets on the left show the locations of the subfigures as hatching rectangles within the study area.

Among the detected 211 sinkholes, 70 emerged before 1945, 51 emerged in 1945–1987, 22 emerged in 1987–2019, 55 appeared in 2019–2022, and 13 appeared between 2022 and 2023. The average areas of the sinkholes developed by the different time of the data acquisition are as follows: by 1945— 99 m² (max. 1956 m² and min. 10 m²), by 1987—68 m² (max. 1059 m² and min. 3 m²), by 2019—42 m² (max. 311 m² and min. 1.3 m²), between 2019 and 2022—27 m² (max. 172 m² and min. 1 m²), and between 2022 and 2023— 8 m² (max. 47 m² and min. 0.7 m²). The highest concentration of sinkholes is

observed in two areas. One area is located 200 m behind the crown of the 2014 landslide, and the second area is located about 100 m from the lake shore.

Four large rockfall deposits can be observed in the 2022 dataset on the snowy surface of the upper part of the caldera wall, which implies their recent occurrence.

Together with instability features, we identified four areas of rugged surface possibly attributed to permafrost processes (see "Discussion" section), which are located in the vicinity of thermal anomalies.
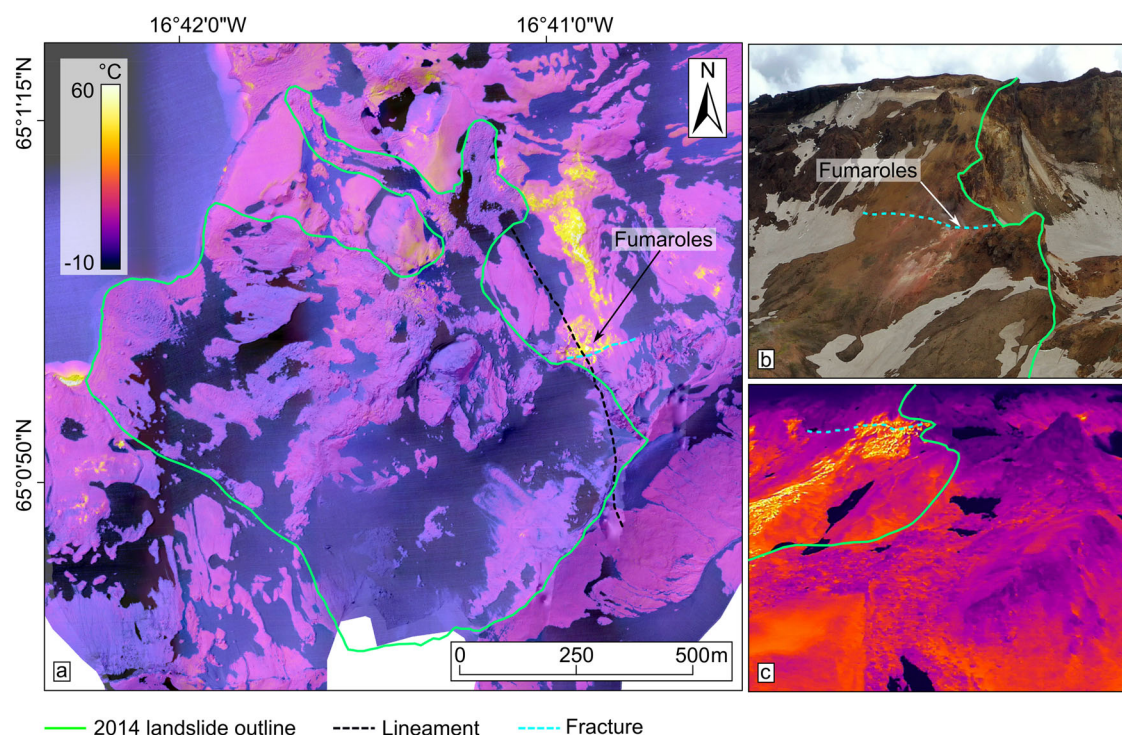
Fig. 5 | The fumarolic field and thermal anomalies at the NE landslide flank. a The 2022 drone infrared orthophoto shows thermal anomalies at the NE flank of the 2014 landslide. **b**, **c** Oblique aerial photographs (2022 visible and 2023 infrared) of the fumarolic field at the NE flank of the landslide.

3D and volumetric analysis of the 2014 and possible future landslides

The 2013 and 2022 Plèiades DEM comparison shows that the main sub-aerial material from the 2014 landslide accumulated in the middle part of the caldera wall while the surface below remains almost intact. The pre-landslide topography (Fig. 8a) shows a bench in the middle of the caldera wall, which may have acted as a barrier in the way of the landslide masses, promoting deposition of the main part in the middle of the slope (Fig. 8b). As we identified in the photogrammetric archives (Fig. 2a), the lower part of the underlying landslide surface was covered by the lava flow, which could together with the steep slope facilitate the rest of the landslide masses sliding down to the water without major impact on the underlying topography. Note that the other detected unstable areas do not have barriers on the lower slopes beneath them.

By subtracting the post-landslide (2022) from the pre-landslide (2013) topography (Fig. 8c, e, f) within the landslide area (718,200 m²) we calculated the volume of the 2014 landslide, which is 11.3×10^6 m³ $\pm 0.3 \times 10^6$ m³ of the removed material (depletion) and 4.8×10^6 m³ $\pm 0.5 \times 10^6$ m³ of the added material (accumulation). Thus, we can consider about 6.5×10^6 m³ to be deposited underwater.

To assess possible future landslide impact we performed a volumetric analysis of the largest unstable area (Fig. 8c, d) by adjusting the artificial sliding plane to the alleged sliding block (see "Methods" section and Supplementary Fig. 13). The possible landslide volume is 8.5×10^6 m³, which is less than the material that slid down in 2014.

Discussion

Askja caldera is a dynamic landform, where post-eruptive morphological and structural changes occur at different temporal and spatial scales. Small changes such as fracture and sinkhole formation can occur unnoticed, but can also be precursors to large and hazardous events like the 2014 landslide. Therefore, it is essential to track the changes at different scales and over a longer time to identify the drivers and precursors of mass wasting and to understand the possible interactions of different processes affecting the stability of the caldera walls.

The slope instability at Askja could be caused by processes related to internal and external forces. The main instability factors and triggers could be the oversteepening of slopes, heterogeneity of deposited material, rock decomposition caused by hydrothermal alteration, seismic activity, etc. Below we discuss the factors that could be supported by surface expressions identified in our dataset.

The Askja caldera walls are mostly steep (>45° in the upper parts (Fig. 2c, d)). Deposits of three pre-1945 landslides were observed as well as several recent rockfalls. Repeated wasting of loose material can promote further oversteepening and de-buttressing of the upper parts of the slopes, which could be composed of more coherent material[36]. Such an upslope migration of instabilities can be assumed from the comparison of the 1945/1987 and 2022 datasets. In the upper part of the area later affected by the 2014 landslide, we can see the pre-1945 landslide material, which originated from the middle part of the eroded body that slid down in 2014 together with a part of the caldera rim (Supplementary Fig. 4b).

The study area contains a large fumarolic field and multiple localized thermal anomalies that promote rock alteration leading to mechanical weakening[37]. The previous results of material classification together with hyperspectral measurements of rock samples[29] showed that the landslide source area is represented by hydrothermally altered material. Our data show that in addition to the current geothermally active sites, there are several areas of past geothermal activity (Supplementary Fig. 6). The fractures in these areas are infilled with altered material, and there are no currently active fumaroles. One such area is located in the middle upper part of the landslide. The fumarolic activity apparently took place there after the 2014 landslide as the vents are expressed. However, it could have started before the event, promoting rock alteration and instability. The largest thermal anomaly (fumarolic field) at the NE flank of the landslide partially matches the observed lineament (Fig. 2c; Fig. 7) and might also have contributed to the slope instability. According to the 1985 Landsat 5 satellite data (Supplementary Fig. 7), the thermal anomalies (thaw patches) appeared in this area decades before the 2014 landslide. Fumaroles and thermal anomalies on one side may change the rocks to grade into mechanically weak soils[38],
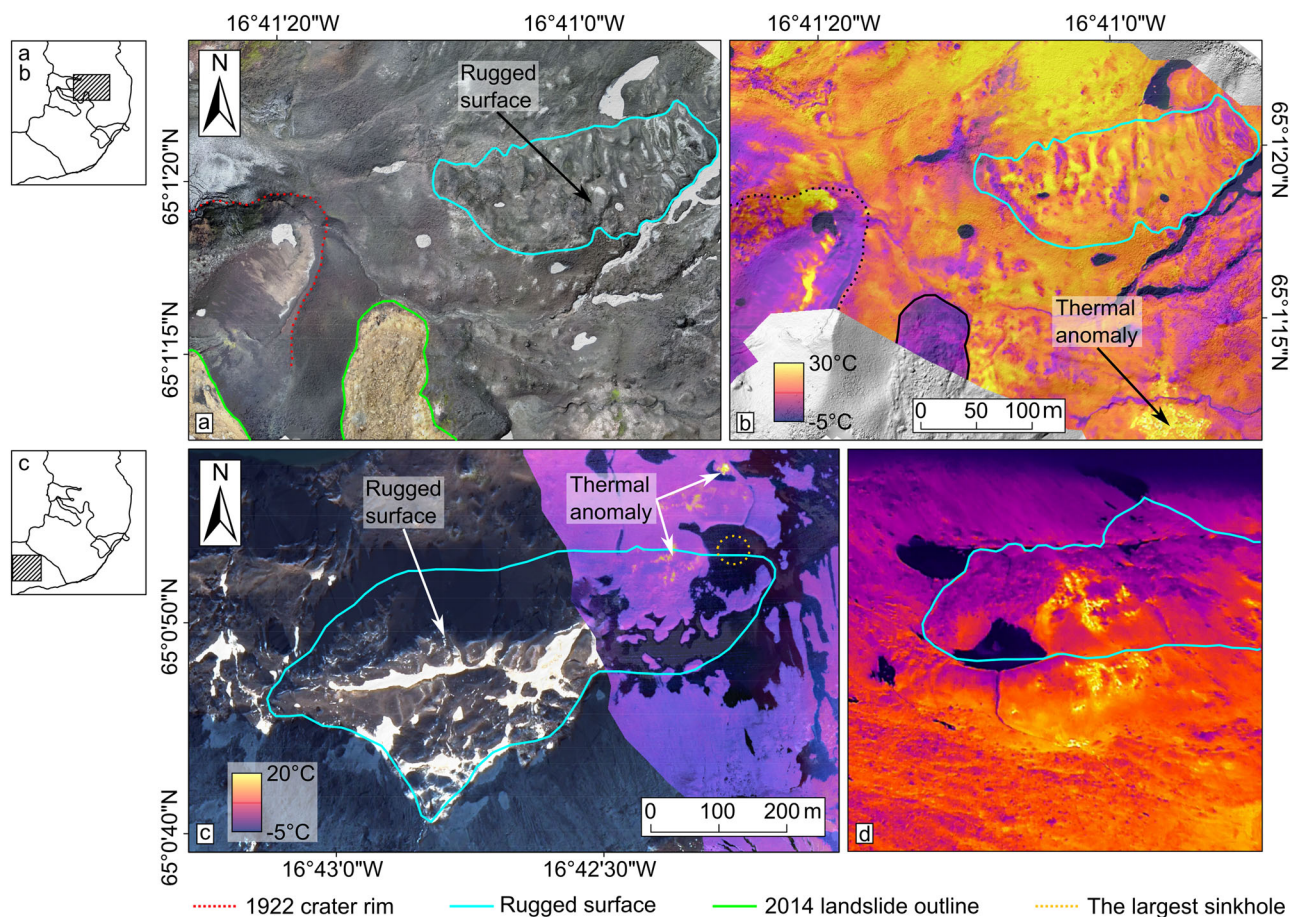
Fig. 6 | Rugged terrains on the SE caldera wall that could be associated with permafrost processes. a Textured DEM of the eastern caldera wall showing folded surface located above the 1922 eruption crater. **b** The same area is shown in the infrared orthophoto. **c** Textured DEM + partial coverage infrared orthophoto of the southern caldera wall showing polygon patterned surface located in the southern part of the study area. **d** Infrared oblique drone image showing the same area (**c**) from NE. Insets on the left show the locations of the subfigures as hatching rectangles within the study area.

and on the other side might melt and destabilize the frozen underground (see also below).

During our 2023 fieldwork, we observed rock fragments of different sizes (from several cm to about 0.5 m) distributed behind the 2014 landslide crown at the outer caldera slope (Supplementary Fig. 8). The fragments are sorted sizewise: larger fragments are closer to the crown. This may indicate a possible explosion during the 2014 event. It was reported[25] that members of a rescue team saw a white plume rising above Askja three minutes after the landslide and that the plume could have resulted from the exposure of the shallow hydrothermal areas abruptly lowering the pressure in the geothermal water. Such rapid release of the pressure could lead to a steam-driven explosion, which can occur when heated water trapped below the surface rapidly converts to steam, disrupting the confining rock. At hydrothermal explosions, boiling water, steam, and rock fragments can be ejected over an area of a few meters up to several kilometers[39,40]. Conversely, a hydrothermal explosion could trigger a landslide when a large amount of meteoric water reaches the overheated interior of the caldera walls. However seismic data revealed no signal before and during the 2014 landslide that can be associated with an explosion[27]. The photogrammetric dataset show several craters on the steep wall at the 1923 vent area; thus the possibility of explosions should be taken into account for future hazard assessment at Askja as they could pose a high risk to visitors and occur without warning[41]. The observed rock fragments are not visible in the 1987 photogrammetric archives (0.4 m resolution); however, this evidence is insufficient to state that the fragments were not there before the landslide.

According to the previous results[30,31], widespread mountain permafrost can be expected in Iceland above 1000 m a.s.l in the south and 800 m a.s.l in

the north and east. Permafrost is probably degrading, as indicated by comparing surface and borehole temperatures. Extensive areas of permafrost are located adjacent to the NE glacier margin of Vatnajokull, including Askja, which may be one of the main spots of permafrost in Iceland over long periods in the Holocene[31]. The recent InSAR study of the large-scale ground deformation in Iceland[23] showed that together with the external plate-boundary deformation, and the isostatic uplift caused by glacier retreat, the widespread deformations can be seen on west- and east-facing slopes leading to the intense landslide activity. It was suggested that slope deformations and intensified landslides can be caused by the degrading permafrost[23,31,42]. In addition, many of Askja's eruptions, including the 1875 caldera-forming eruption, occurred during the late winter/early spring season, which is why volcanic material was deposited on thick layers of snow and ice[43].

Therefore, together with deep-seated permafrost that can reach 600 m in thickness (from 800 m to 1400 m a.s.l) at Askja, a layer of underground ice buried by loose volcanic deposits can be observed today in the area of the NW lava field (Supplementary Fig. 9). Similar buried ice was exposed at the SE caldera rim after being outcropped by the 2014 landslide, where it reached about 10 m thickness (Fig. 9a). Under this layer of ice, two surface water discharge areas can be observed. They could indicate that the water from the melting outcropped ice flows along nonpermeable rock or frozen ground. The layers of buried ice up to 4.4 m thick were surveyed with ground-penetrating radar through the 1875 and 1961 deposits in the NE part of Askja[43]. If there were no frozen ground underneath these layers of ice, they would likely have melted within the last few decades. Therefore, we suggest that cryosphere at Askja can be present at different scales: as
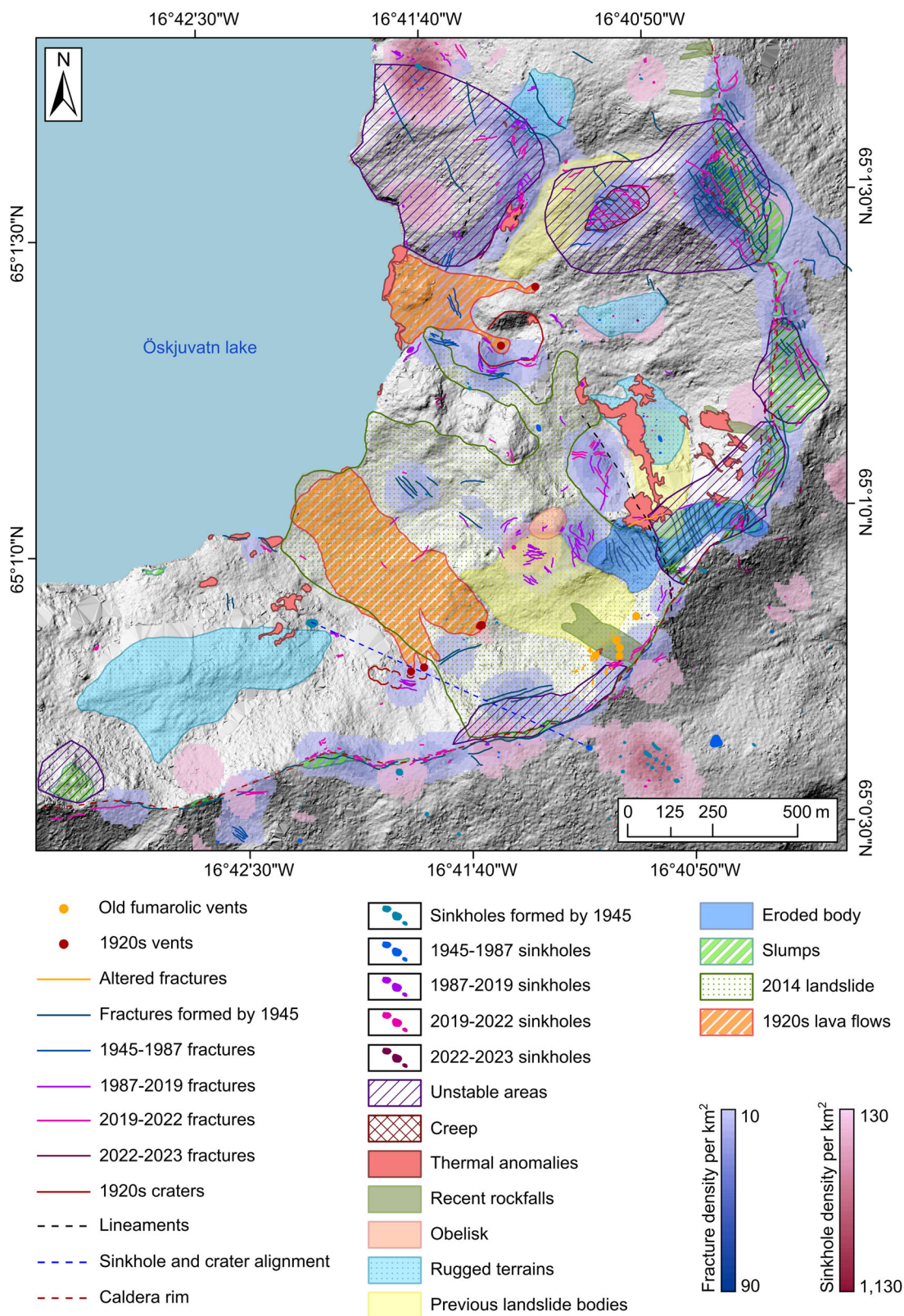
Fig. 7 | Hillshade map based on the results of the 1945-2023 photogrammetric data interpretation. The map shows eruptive, instability and cryospheric features identified in the SE caldera wall since 1945, as well as newly emerged features identified in the later (1987–2023) datasets. The hillshade base is generated from the 2022 Plèiades DEM.

deep-seated mountain permafrost localizations, and as layers of buried ice at the shallow level.

    Another phenomenon that can be observed at Askja is buried snow formation on the steep slopes due to the repeated coverage of the recent snow with scree and rockfall material (Fig. 9b), which could lead to rock

glacier formation. Such a feature can be observed at the southern wall of Askja with a typical glacier crevasse (Supplementary Fig. 10).

    Our assumption that the identified rugged terrains relate to periglacial processes based on their strong morphological similarities to permafrost features and patterned ground elsewhere (Fig. 9c–h). The eastern rugged
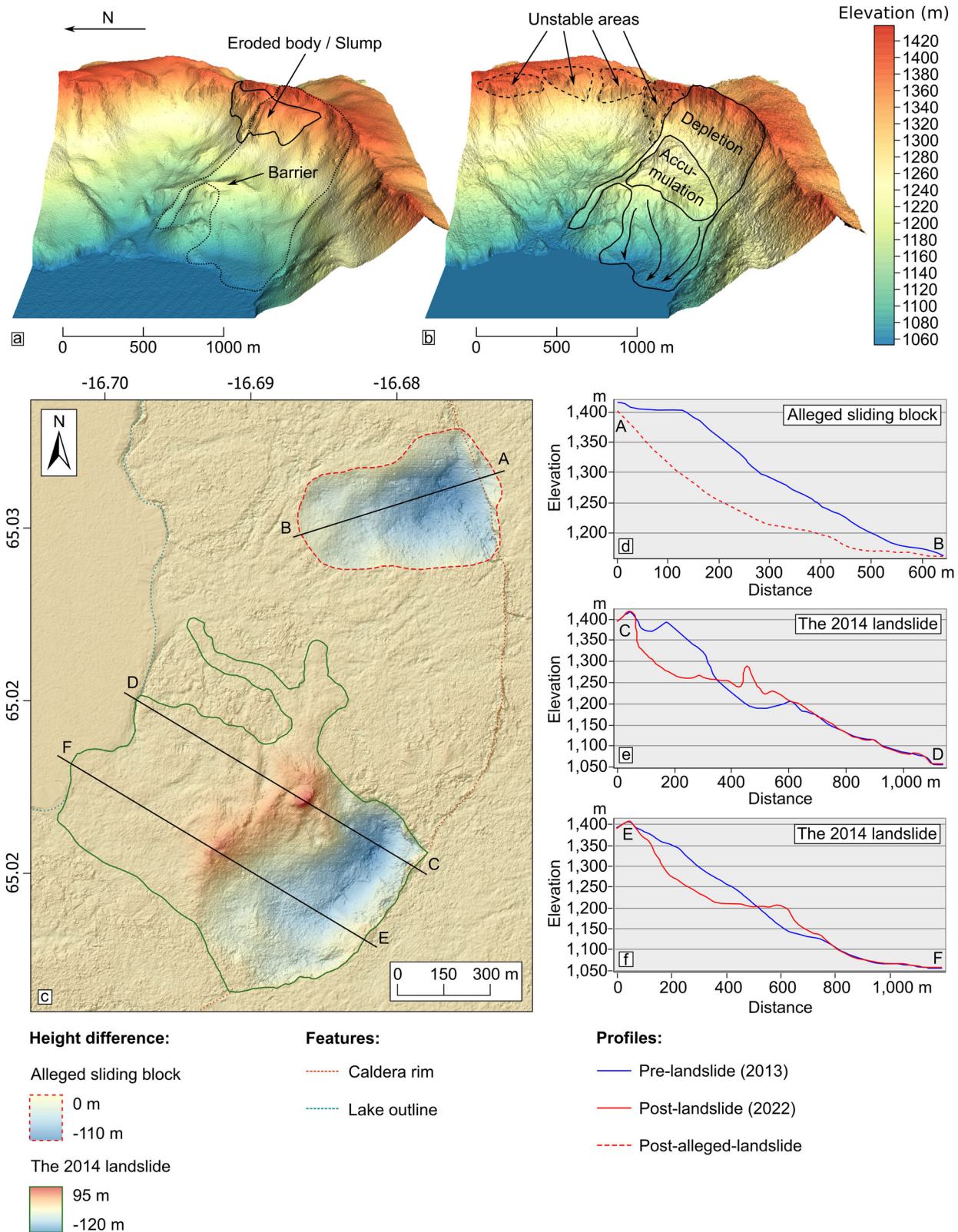
Fig. 8 | The 3D comparative analysis of the pre- and post-landslide topographies. **a** Topography generated from the 2013 Plèiades dataset, showing a bench in the middle of the wall that could prevent the complete sliding of the upper parts of the wall into the lake. **b** Topography generated from the 2022 Plèiades dataset, showing that the main subaerial landslide material accumulated in the middle of the wall (above the underlying bench). **c** The difference DEM map of the 2014 landslide (lower area) and the alleged sliding block (upper area). **d–f** Pre- and post-landslide profiles along the lines AB, CD, and EF taken from 2013 and 2022 Plèiades data. Note that the details of the alleged sliding block are hypothetical, although structural features indicate flank instability at this site and demand for close monitoring and further studies.
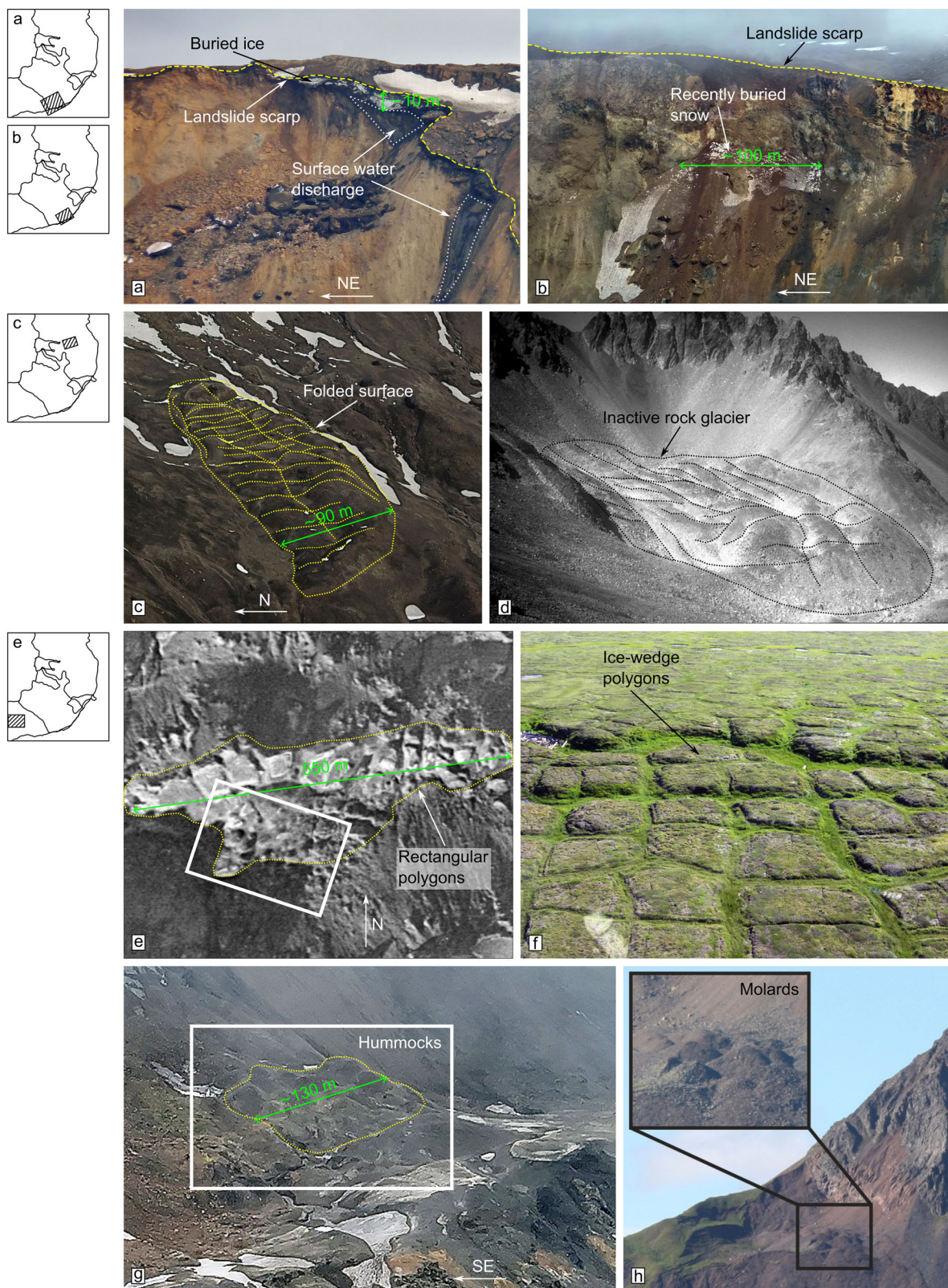
terrain (Figs. 6a and 9c) has longitudinal and compressional ridges and morphology of an inactive or relict rock glacier (Fig. 9d[44]). It is located just above the vent area of the Kvíslahraun lava flow and could be attributed to the permafrost activity (thawing) during the 1922/23 unrest and volcanic heat propagation. This rugged terrain shows no movement throughout our dataset, indicating that there has been no permafrost activity in this area since 1945. Another rugged terrain located on the SE wall of Askja (Figs. 6c and 9e) shows symmetrical polygons that bear similarities with ice-wedge polygons in northern Yukon permafrost peatlands (Canada) (Fig. 9f[15]). In the upper (southern) part of this rugged terrain typical molards can be observed (Fig. 9g), which are conical features that originate from frozen ground blocks moved with mass wasting downslope from their original

Fig. 9 | Morphological features of Askja caldera walls can be associated with cryospheric processes. a A 10-m-thick layer of buried ice in the upper part of the caldera wall outcropped by the 2014 landslide; under the layer and lower on the slope two surface water discharges can be observed; photo courtesy of Dave McGarvie (Lancaster University). The photo was taken on 26.07.2014, 5 days after the landslide; in the later photographs, the layer of ice is not visible in this area. **b** Buried snow formation on the steep headwall of the 2014 landslide through repeated deposition of scree material on the snowy surface. **c** The folded surface located at the eastern wall of Askja shows numerous longitudinal and compressional ridges with depressions between them. **d** Similar surface structures can be observed on the inactive rock glacier located at Olympus Range (New Zealand); reprinted from J. Geophys. Res., 108, 8032, Whalley W.B. and Azizi F., Rock glaciers and protalus landforms: Analogous forms and ice sources on Earth and Mars, p. 8, ©2003 by the American Geophysical Union, with permission from John Wiley and Sons[44]. **e** Rectangular polygons at the SE wall of Askja; white rectangle shows the location of **(g)**. **f** Ice-wedge permafrost polygons in northern Yukon permafrost peatlands (Canada); reprinted from Quaternary Science Reviews, 147, M. Fritz et al., Holocene ice-wedge polygon development in northern Yukon permafrost peatlands (Canada), p. 281, ©2016 Elsevier Ltd., with permission from Elsevier[45]. **g** Hummocky surface located at the upper part of the southern rugged terrain at Askja. **h** Molards located at the upper part of Árnesfjall landslide (Iceland); amended from Earth and Planetary Science Letters, 516, Morino et al., Molards as an indicator of permafrost degradation and landslide processes, p. 137, ©2019 The Authors, published by Elsevier B.V. under the CC BY license[46]. Insets on the left show the locations of the subfigures as hatching rectangles within the study area.

position and became unfrozen at the place of deposition. Askja molards can be compared with molards at Árnesfjall landslide (Fig. 9h[46]) located in a permafrost environment[46].

All the identified areas with surface expressions reminiscent of permafrost features are located in the vicinity of thermal anomalies, leaving us to speculate about possible interactions. In active volcanic environments, the perennial ice and permafrost thawing could be caused not only by average atmospheric temperature increase but also by the emergence/increase of volcanic heat flow. The rugged terrain features could have emerged during the 1922/23 unrest when intense heat flow caused permafrost thawing and thus led to the appearance of surface expressions. After the volcanic activity ceased these features became inactive (presence of permafrost without thawing) or relict (absence of permafrost).

In the case of volcanic interaction with permafrost, the thawing can occur at a deeper level leading to the (1) formation of thawed ground overlaid by frozen ground and thus to de-buttressing and slumping of the upper parts of the slopes; (2) moisture accumulation and hydrothermal rock alteration, which promotes instability; and (3) water discharge through the underground channels[47]. Openings of the underground channels can be observed in the middle and lower parts of the caldera wall (Supplementary Fig. 11) and may be an indication of the presence and thawing of deeper permafrost.

The analysis of our dataset revealed that the slope movements at the SE Askja wall are preceded and accompanied by multiple fractures and sinkhole formation. The sinkholes can emerge due to local tectonics—faults formation and reactivation[48] or due to thermokarst processes[49]. It is difficult to distinguish the origin of a particular sinkhole in remote sensing data. However, the specific alignment of some of them (alignment in Fig. 7) can suggest a relation to the local tectonics. In other cases, the sinkholes are clustered without a specific alignment (sinkhole high-density spots in Fig. 7) and could be attributed to the thawing of buried ice.

The source of the 2014 landslide was partially located above the 1923 (Suðurbotnahraun) vents, as well as the large slump at the caldera rim (Fig. 3c) that partially slid down in 2014. The heat flow from the feeder dyke of the 1923 eruption could have contributed to the reduction of the above layer of buried ice as well as possibly deep-seated permafrost and thus could lead to instability at the upper parts of the caldera wall. The largest investigated unstable area, the slump to the north from the 2014 landslide (Figs. 3d and 7), is located above the 1922 (Kvíslahraun) vents and could also be formed due to the heat flow from the eruption.

Our observations let us suggest that (1) Askja is a site of barely understood hydrothermal-permafrost-slope instability interactions, (2) active permafrost processes are ongoing today at Askja and were more intense during the 1922/23 unrest, (3) the permafrost interacting with geothermal activity is coupled to fracture zones, possibly providing the required permeability and pore space, and (4) these interactions could contribute to the increasing instability of the caldera walls already induced by climate change.

The oversteepened walls of the recently formed caldera are subject to intense denudation. Material removal with repeated rockfalls can promote further oversteepening and de-buttressing of the upper parts of the slopes. In

case of effusive activity, heat flow from a propagating dike can interact with buried ice and/or deep-seated permafrost causing them to thaw. The thawing permafrost leads to reduced cohesion and increased pore water pressure in loose material of the heterogenous caldera wall. Besides, the dike opening can cause horizontal deformation by pushing the flank toward the lake and lead to de-buttressing of the upper part of the wall (Fig. 10a). The heat flow interacting with meteoric water leads to intense rock alteration and weakening, which promotes instability and causes tensile fracturing and slumping (Fig. 10b) observed in our dataset. The post-magmatic geothermal activity further affects the rock properties and permafrost state and together with local tectonics leads to the emergence of multiple fractures and sinkholes. The major exogenous factor of cryosphere degradation—the general rise of atmospheric temperature since the 1960s[30]—can likely contribute to slope instability at Askja. The subsidence that was detected within Askja in the 1980s–2021 could also affect the stability of the SE wall. Thus, in July 2014, all the described factors could lead to exceeding the stability threshold and to the major mass-wasting event (Fig. 10c) with cascading hazards - tsunami and possible hydrothermal explosion.

There are many factors of instability of the Askja caldera walls and potential triggers that could cause cascading hazards at any time. The fracturing and slumping can be observed almost everywhere along the SE caldera rim (Supplementary Fig. 12). New cracks and sinkholes appeared throughout the entire study period and slope motion is observed. Three pre-1945 landslide deposits are visible on the caldera wall, which implies that landslides are common at Askja.

Our results show that the impact of the 2014 landslide was reduced due to the bench in the middle of the caldera wall that had underlain the landslide source region acting as a barrier in the way of the landslide masses. Other unstable areas do not have such a barrier beneath them and, in case of future instability events, the rock masses could slide down unhindered to the lake producing larger tsunamis and affecting more areas. This situation requires constant monitoring of the unstable areas taking into consideration all the possible factors and triggers discussed above. Specifically, the investigation of the buried ice and deeper permafrost should be done in near future, as thermokarst and thawing permafrost are considered to be major factors of slope instability[50].

The repeated high-resolution observations could reveal such morphological precursors of preparing mass wasting as appearing and expanding tensile cracks and sinkholes. The location of the 2014 landslide in the Kamchatkan Geysers Valley was successfully predicted in 2009 based on the detection of tensile cracks in the later landslide crown area[51]. The multisensor remote and on-site monitoring could minimize the risks from possible hazardous events in Askja Caldera, which is a tourist hotspot.

Conclusions

We performed photogrammetric processing and analysis of the high-resolution datasets covering the Askja caldera SE wall over the nearly 80-year period that allowed us to reveal and record multiple eruptive and instability features associated with various past and ongoing processes. Our datasets showed that landslides are common at Askja, as three more pre-1945 landslide deposits were identified. We detected the ongoing creeping

Fig. 10 | Conceptual model of processes affecting the stability of the Askja caldera wall presented at different stages of morphodynamics. a Alleged profile of the SE wall during the 1920s effusive activity. The inset shows the profile line within the study area. **b** Amended profile through the 2013 surface showing post-slump topography. **c** Amended profile through the 2022 surface showing post-landslide topography.
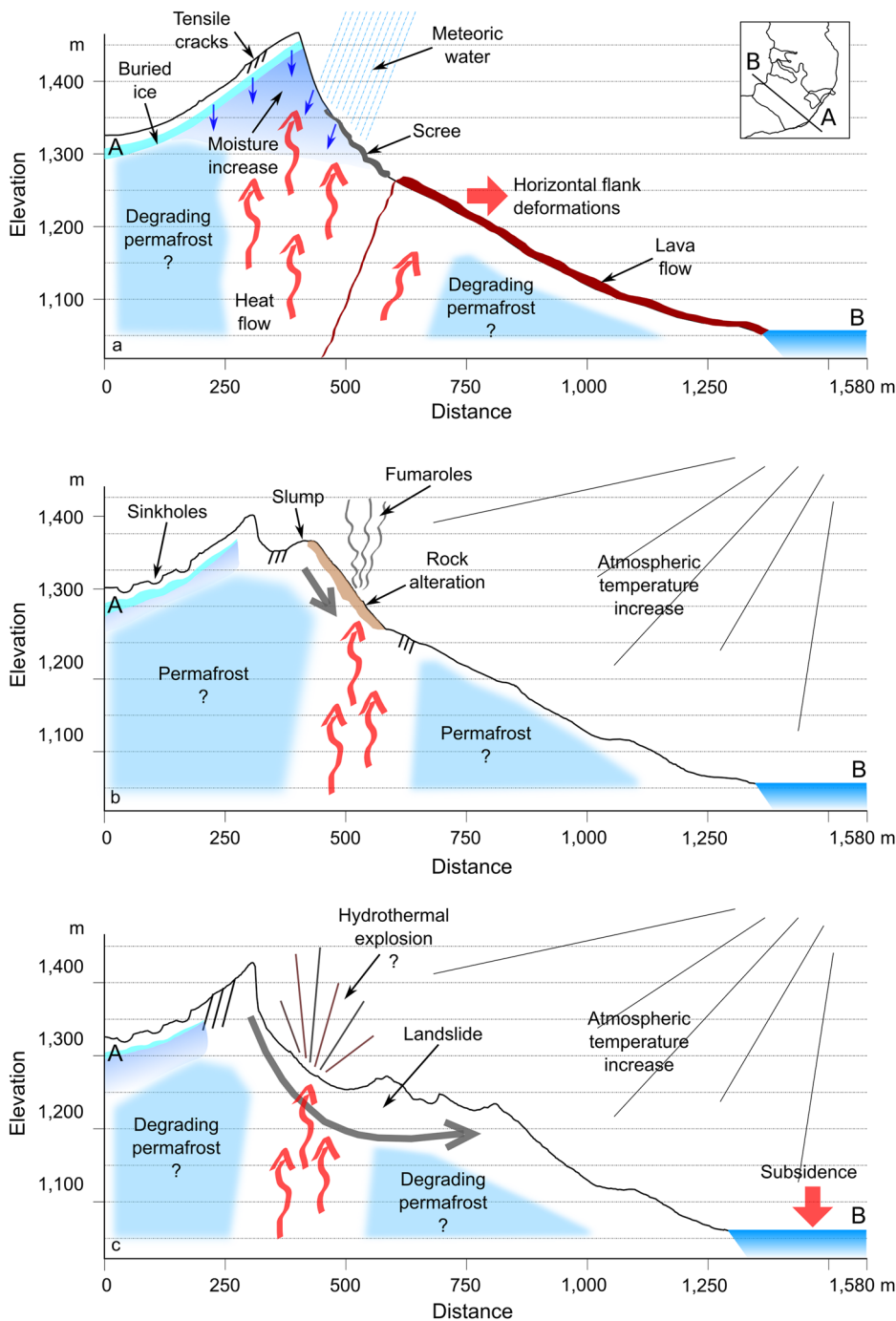
and slumping at some areas of the wall together with emerging and expanding tensile fractures and sinkholes.

The possibility of investigating the pre-2014 landslide morphology that no longer exists allowed us to better understand the specific deposition of the landslide masses and make assumptions regarding future hazardous events. We revealed that the 2014 mass wasting was constrained by the preexisting topography, which reduced the landslide and tsunami impact. Other detected unstable areas do not have such constraints and future mass wasting could lead to more severe hazards.

The main factors and triggers of slope instability at Askja could be the oversteepening of the upper parts of the caldera walls, intense rock alteration, hydrothermal explosions, etc. Besides, we emphasize the possible effect of cryosphere degradation on the stability of the caldera walls and assume

that the observed slumps at the caldera rim could be related to the effusive activity of the 1920s. We address the unstudied phenomenon of volcanic heat and permafrost interaction and show that it can play an essential role in the morphological evolution of Askja caldera.

We suggest that the unstable situation at Askja, a popular tourist destination in summer, can pose a high risk to visitors and requires remote sensing and on-site monitoring to detect morphological (emerging and expanding fractures and sinkholes) and other precursors of the preparing mass wasting.

Methods

We employ an 80-year remote sensing dataset (Supplementary Fig. 1), which allows us to investigate the morphological changes at the SE wall of

Askja caldera. In the following, we provide a background on photogrammetry, followed by a description of data and processing methods used in this work.

Photogrammetric processing

Photogrammetry is a technique for obtaining quantitative information about physical objects from their photographic images[52]. The main processing algorithms include (1) interior orientation, which establishes the relationship between the image plane and the projection center of a camera using such camera parameters as focal length and pixel (frame) size; (2) relative orientation, which restores the position and orientation of one image with another using tie points; (3) exterior orientation, which establishes the relationship between the image and the surveyed surface; (4) virtual 3D terrain extraction, which calculates the 3D coordinates of each point of a generated point cloud that corresponds to a specific point on the ground. Thus, through photogrammetric processing of acquired overlapping visible and infrared images, we can create a precise and georeferenced 3D surface and orthophoto map of the study object. Photogrammetric processing can be performed in different software packages; in this study, we used Agisoft Metashape Professional v. 1.8.3, which automates the above-mentioned steps and simplifies photogrammetric processing[53]. The processing in Metashape includes several steps: (1) photo alignment, which consists of aerial triangulation and bundle block adjustment (relative orientation) and estimates the interior and exterior camera orientation parameters. The result of the alignment is a tie point cloud, which is necessary for the determination of the depth maps; (2) generation of a 3D surface on the base of the depth maps, which can be a dense point cloud, a mesh, or a raster DEM. A DEM can be based also on the dense point cloud data instead of the depth maps; (3) referencing with ground control points (GCPs) (if required); and (4) orthophoto generation. Below, we describe the photogrammetric processing of our multisensory datasets.

Archive aerial

The National Land Survey of Iceland started conducting surveys in the 1950s using small-format images (18×18 cm, focal length 115 mm). These were replaced by standard aerial mapping cameras from the 1970s onwards (23×23 cm, focal length 153 mm). Such standard cameras were used in the American Mapping Service (AMS) surveys covering the whole of Iceland in 1945–1946 and 1956–1961. A forward overlap of 60% was generally used. Most of these data are publicly available in digital form on the LMI online database while some sets are available upon request[54].

In this work, we used aerial photographs acquired on 30.08.1945 and 06.08.1987 as they fully cover the area of interest. The 1945 dataset consists of 4 images acquired in one flight path with a 6700 m flight altitude, 153.3 mm camera focal length, 23×23 cm frame size, and 60% forward overlap. The 1987 dataset consists of 5 images that cover only the eastern side of the caldera. The images were acquired from a 6100 m flying height, with 151.78 mm focal length, 23×23 cm frame size, and 60% forward overlap. During the image alignment in Metashape, 4500 tie points were generated for the 1945 dataset and about 5700 for the 1987 dataset. The georeferencing was performed with 15 GCPs that were set in the images around the caldera at distinctive topographic features; the coordinates for the markers were obtained from the 2022 Plèiades DEM (see next subsection) where the same topographic features can be recognized in the images. The maximum reference error provided by Metashape is 0.1 m (for the 1945 set) and 0.4 m (for the 1987 set). The same technique of georeferencing was previously used by Shevchenko et al.[6,55]. The resulting point clouds and DEMs have a resolution of 2.1 m (1945) and 1.4 m (1987), and the resolution of orthophotos is 1 m (1945) and 0.4 m (1987). The data are referenced to the WGS84 coordinate system, 27 N UTM zone. Note that the quality of DEMs generated from archive aerial data is not sufficient enough for the complete 3D analysis of the pre-landslide topography (see Supplementary Discussion).

Plèiades

For precise topography reconstruction before and after the 2014 landslide, we used two sets of Plèiades satellite images (panchromatic—0.5 m-res and multispectral—2.5 m-res) acquired on 16.06.2013 (stereo images) and on 27.08.2022 (tri-stereo images) that cover the entire Askja caldera. The data were processed in the same way as described in the previous subsection, except for the geo-referencing, which was performed automatically based on Rational Polynomial Coefficient data with a maximum reference error of 0.3 m. The obtained point clouds and DEMs have a 1 m resolution for panchromatic data and about 5 m for multispectral data; the orthophotographs have 0.5 m and 2.5 m in resolution respectively. The multispectral Plèiades orthophotos were pan-sharpened[56] with ArcGIS desktop v. 10.8.2 Pan-sharpening tool using the corresponding panchromatic orthophotos. The 2022 Plèiades DEM was used as a reference base for the archive dataset (see previous subsection).

Drone visible

We used three sets of drone data acquired on 28.08.2019, 15.07.2022, and 26–28.07.2023. The 2019 data were collected with a DJI Inspire1 quadcopter with a Zenmuse X3 Full HD camera onboard. The resolution of the camera is 12 MP, and the pixel size is 1.5 μm. The 4000×3000 px images were acquired during 4 overflights at 600 m flight altitude above the lake level resulting in a 17 cm average ground resolution.

To acquire the 2022 data, we used a DJI Phantom 4 RTK quadcopter with more precise positioning enabled using a ground station and equipped with a 1-inch CMOS RGB camera of 20 MP with 2.41 μm pixel size onboard. We flew the drone at an altitude of 500 m above the caldera lake surface and took images with an 80% forward and 60% sideward overlap. The images were acquired with a resolution of 5472×3648 px and about 7 cm ground resolution on average, depending on the distance to the surface. In total, we conducted 6 overflights to cover the landslide area and the upper flanks.

In 2023, due to the poor weather conditions, we did not manage to capture the whole landslide area, and our dataset is in the form of eight separate patches over the landslide and adjacent caldera rim areas. For acquisition, we used a DJI Mavic 3T quadcopter with 48 MP and 3.3 μm pixel size 1/2" CMOS camera onboard with a flight height of 470–580 m above the caldera lake (different altitudes for different patches). The pixel and ground resolutions of the images are 8000×6000 px and 7–16 cm respectively.

The photogrammetric processing of all acquired drone imagery was similar for all drone datasets. Before the processing, we checked the image quality by visual inspection and removed blurry images. The remaining images were imported into Metashape. For the processing steps, we followed the standard Metashape workflow. Firstly, we performed image alignment and generated tie points. Secondly, we generated depth maps and high-quality 3D dense clouds. Afterward, we continued the processing by generating ultra-high-resolution DEMs and orthophotos.

Drone infrared

To locate thermal anomalies and compare them to observed morphological features, we also used drone-based infrared data. During our field campaign in 2022, and 2023, we acquired thermal images of the landslide and adjacent areas together with photogrammetric surveys using a FLIR-TAU 2 camera with a TEAX ThermalCapture frame grabber attached to the drone in 2022 and DJI Mavic 3T embedded thermal camera in 2023.

The FLIR-TAU 2 records 640×512 px radiometric images in the thermal infrared range (7.5–13 μm) at 8 Hz, which makes it ideal for surveying apparent ground temperatures during flight. The camera was calibrated to the temperature range between -40 °C to 180 °C. The acquired images were pre-processed in ThermoViewer v. 3.0.4, corrected for thermal emissivity (95%) and environmental path temperatures (10 °C), and exported in JPG format for further photogrammetric processing.

The DJI Mavic 3T thermal camera acquired 640×512 px radiometric images within 8–14 μm infrared wavelength at 8 Hz. We used the apparent

temperature range of −40 °C to 180 °C and thermal emissivity of 95%. We pre-processed the images in DJI Thermal Analysis Tool v. 3.1.0.

The images from each dataset were then further integrated into the photogrammetric processing using Metashape (see Photogrammetric processing section) to create a 3D surface model and orthophoto map with colors corresponding to apparent ground temperature values. The resulting infrared orthophoto mosaics have a ground resolution of 55 cm in 2022, and 15–40 cm for different patches in 2023.

Note that the temperatures presented in this work are the apparent temperatures measured from our sensor, which may be affected by hydrometeorological conditions, emissivity, pixel-to-anomaly size ratio, etc. The values presented might therefore underestimate the real fumarole temperatures. We use the thermal data for a spatial constraint of thermal anomalies only. A quantification of the real vent temperatures or thermal radiation is beyond the scope of this work (see Supplementary Discussion).

Data alignment and error estimation

The resulting 2022 Plèiades point cloud was aligned to the point cloud generated from the 2016 ÍslandsDEM (LMI) to improve the absolute accuracy and further served as a reference for all other photogrammetric data. The coordinates extracted from the Plèiades data were used for referencing the archive aerial data in Metashape with distributed markers (see Archive aerial subsection). However, the archive point clouds still had several meters shift in roll, pitch, and yaw axis as well as non-RTK drone point clouds. That is why we performed further alignment with the Finely registration tool in CloudCompare v. 2.9.1 to stack all used point clouds, similar to the previous study[6]. We generated new DEMs from the aligned point clouds using the Create LAS Dataset and LAS to Raster tools of ArcGIS. The relative alignment errors were calculated by comparing Z distances between two DEMs measured at several points distributed in different areas not affected by the landslide. Using the extracted Z differences at the distributed points, we calculated Root Mean Square Errors (RMSEs) of the DEMs' relative alignment (Supplementary Table 1).

The orthophotos (except for those acquired by Plèiades sensor and taken with RTK drones) also had a several-meter shift and thus, were also aligned to the 2022 Plèiades orthophoto with the Shift function in the Georeferencing tool of ArcGIS so that they visually match each other at a large-scale (zoomed) view.

Volumetric analysis

To analyze changes that occurred between 2013 and 2022, we performed a comparative analysis of the Plèiades point clouds and calculated the volumetric difference. First, we improved the relative adjustment of the two point clouds with RMSE of 1.2 m (see previous section). Then the volume of the 2014 landslide was calculated using the Compute 2.5D Volume tool of CloudCompare. The obtained RMSE was distributed over the area of the landslide separately for the depletion area (265,300 m^2; 318,360 m^3) and accumulation area (452,900 m^2; 543,480 m^3) to estimate the volume errors for the removed (2 %) and added (9 %) material. To estimate the volume of the alleged future landslide (see 3D and volumetric analysis of the 2014 and possible future landslides in "Results"), we adjusted an artificial sliding plane to the displaced block (slump) at the caldera rim on the 2022 point cloud (Supplementary Fig. 13) and calculated the volumetric difference between them. The sliding plane was taken from the point cloud of the upper part of the adjacent caldera wall.

GIS mapping

The products obtained from the processing (DEMs, visible, and infrared orthophotos) were stacked in an ArcGIS project and further post-processed and visually analyzed. Based on the DEMs, hillshade and slope maps were generated using ArcGIS tools. The morphological features (landslides, vents, fractures, sinkholes, etc.) were visually identified in the hillshades and orthophotos and were outlined and recorded as shapefiles. The multitemporal dataset analysis allows us to identify and map the newly emerged features (fractures and sinkholes). The resulting maps were exported and further elaborated in the graphic editor Inkscape v. 0.92.4.

Data availability

References

1. Francis, P. W., Gardeweg, M., Ramirez, C. F. & Rothery, D. A. Catastrophic debris avalanche deposit of Socompa volcano, northern Chile. *Geology* **13**, 600–603 (1985).
2. Cole, J. W., Milner, D. M. & Spinks, K. D. Calderas and caldera structures: a review. *Earth Sci. Rev.* **69**, 1–26 (2005).
3. Moore, J. G. et al. Prodigious submarine landslides on the Hawaiian Ridge. *J. Geophys. Res. Solid Earth* **94**, 17465–17484 (1989).
4. van Wyk de Vries, B. & Francis, P. W. Catastrophic collapse at stratovolcanoes induced by gradual volcano spreading. *Nature* **387**, 387–390 (1997).
5. Walter, T. R. et al. Complex hazard cascade culminating in the Anak Krakatau sector collapse. *Nat. Commun.* **10**, 4339 (2019).
6. Shevchenko, A. V. et al. Constructive and destructive processes during the 2018–2019 eruption episode at Shiveluch Volcano, Kamchatka, studied from satellite and aerial data. *Front. Earth Sci*. **9**. https://doi.org/10.3389/feart.2021.680051 (2021).
7. McGuire, W. J. Volcano instability: a review of contemporary themes. *Geol. Soc. Lond. Spec. Publ.* **110**, 1–23 (1996).
8. Tuffen, H. How will melting of ice affect volcanic hazards in the twenty-first century? *Philos. Trans. J. Soc. A Math. Phys. Eng. Sci.* **368**, 2535–2558 (2010).
9. Lipman, P. W. Magmatism in the Cordilleran United States; progress and problems. *The Cordilleran Orogen*. https://doi.org/10.1130/DNAG-GNA-G3.481 (1992).
10. Lipman, W. P. Calderas. in *Encyclopedia of volcanoes*. (ed. Sigurdsson, H.) 643–662 (Academic Press, 2000).
11. Merle, O., Michon, L. & Bachèlery, P. Caldera rim collapse: a hidden volcanic hazard. *J. Volcanol. Geotherm. Res.* **177**, 525–530 (2008).
12. Nakada, S., Nagai, M., Kaneko, T., Nozawa, A. & Suzuki-Kamata, K. Chronology and products of the 2000 eruption of Miyakejima Volcano, Japan. *Bull. Volcanol.* **67**, 205–218 (2005).
13. Burchardt, S. & Walter, T. R. Propagation, linkage, and interaction of caldera ring-faults: comparison between analogue experiments and caldera collapse at Miyakejima, Japan, in 2000. *Bull. Volcanol.* **72**, 297–308 (2010).
14. Geshi, N., Shimano, T., Chiba, T. & Nakada, S. Caldera collapse during the 2000 eruption of Miyakejima Volcano, Japan. *Bull. Volcanol.* **64**, 55–68 (2002).
15. Thordarson, T. & Larsen, G. Volcanism in Iceland in historical time: volcano types, eruption styles and eruptive history. *J. Geodyn.* **43**, 118–152 (2007).
16. Graettinger, A. H. et al. Remote sensing and geologic mapping of glaciovolcanic deposits in the region surrounding Askja (Dyngjufjöll) volcano, Iceland. *Int. J. Remote Sens.* **34**, 7178–7198 (2013).
17. Trippanera, D., Ruch, J., Acocella, V., Thordarson, T. & Urbani, S. Interaction between central volcanoes and regional tectonics along divergent plate boundaries: Askja, Iceland. *Bull. Volcanol*. **80**. https://doi.org/10.1007/s00445-017-1179-8 (2018).
18. Hartley, M. E. & Thordarson, T. The 1874–1876 volcano-tectonic episode at Askja, North Iceland: lateral flow revisited. *Geochem. Geophys. Geosyst.* **14**, 2286–2309 (2013).
19. Thorarinsson, S. & Sigvaldason, G. E. The eruption in Askja, 1961; a preliminary report. *Am. J. Sci.* **260**, 641–651 (1962).

20. Tryggvason, E. Ground deformation in Askja, Iceland: Its source and possible relation to flow of the mantle plume. *J. Volcanol. Geotherm. Res.* **39**, 61–71 (1989).

21. Koymans, M. R. et al. Decades of subsidence followed by rapid uplift: Insights from microgravity data at Askja Volcano, Iceland. *J. Volcanol. Geotherm. Res.* **442**, 107890 (2023).

22. de Zeeuw-van Dalfsen, E., Pedersen, R., Hooper, A. & Sigmundsson, F. Subsidence of Askja caldera 2000–2009: Modelling of deformation processes at an extensional plate boundary, constrained by time series InSAR analysis. *J. Volcanol. Geotherm. Res.* **213–214**, 72–82 (2012).

23. Cao, Y., Jónsson, S. & Hreinsdóttir, S. Iceland kinematics From InSAR. *J. Geophys. Res. Solid Earth* **128**, e2022JB025546 (2023).

24. Parks, M. M. et al. 2021–2023 unrest and geodetic observations at Askja Volcano, Iceland. *Geophys. Res. Lett.* **51**, e2023GL106730 (2024).

25. Saemundsson, T., Helgason, J. K., Brynjolfsson, S. & Hoskuldsson, A. *The rockslide in the Askja caldera on the 21st of July 2014*. Vol. 17, 11734 (EGU General Assembly 2015, 12-17 April 2015 Vienna, Austria, 2015).

26. Gylfadóttir, S. S. et al. The 2014 Lake Askja rockslide-induced tsunami: optimization of numerical tsunami model using observed data. *J. Geophys. Res. Ocean.* **122**, 4110–4122 (2017).

27. Schöpa, A. et al. Dynamics of the Askja caldera July 2014 landslide, Iceland, from seismic signal analysis: precursor, motion and aftermath. *Earth Surf. Dynam.* **6**, 467–485 (2018).

28. Elíasson, J. & Sæmundsson, Þ. Physics and Modeling of Various Hazardous Landslides. *Geosciences* **11**. https://doi.org/10.3390/geosciences11030108 (2021).

29. Marzban, P. et al. Hydrothermally altered deposits of 2014 Askja landslide, Iceland, identified by remote sensing imaging. *Front. Earth Sci.* **11**. https://doi.org/10.3389/feart.2023.1083043 (2023).

30. Etzelmüller, B. et al. The regional distribution of mountain permafrost in Iceland. *Permafr. Periglac. Process.* **18**, 185–199 (2007).

31. Etzelmüller, B. et al. Icelandic permafrost dynamics since the Last Glacial Maximum—model results and geomorphological implications. *Quat. Sci. Rev.* **233**, 106236 (2020).

32. Chen, X., Sun, Q. & Hu, J. Generation of Complete SAR Geometric Distortion Maps Based on DEM and Neighbor Gradient Algorithm. *Appl. Sci.* **8**. https://doi.org/10.3390/app8112206 (2018).

33. Shevchenko, A. V., Walter, T. R., Belart, J. M. C., Marzban, P. & Zorn, E. U. Askja caldera 1945-2023 *geospatial dataset*. https://doi.org/10.5281/zenodo.12686925 (2024).

34. Gylfadottir, S. S. et al. Haettumat vegna berghlaupa í Öskju. *Veðurstofa Íslands Skýrsla.* **2016-007**, 49 (2016).

35. Helgason, J. K. et al. Berghlaupið í Öskju 21. júlí 2014. *Náttúrufræðingurinn* **89**, 5–21 (2019).

36. Friele, P. A. & Clague, J. J. Large Holocene landslides from Pylon Peak, southwestern British Columbia. *Can. J. Earth Sci.* **41**, 165–182 (2004).

37. Heap, M. J. & Violay, M. E. S. The mechanical behaviour and failure modes of volcanic rocks: a review. *Bull. Volcanol.* **83**, 33 (2021).

38. Heap, M. J. et al. Quantifying the role of hydrothermal alteration in creating geothermal and epithermal mineral resources: the Ohakuri ignimbrite (Taupō Volcanic Zone, New Zealand). *J. Volcanol. Geotherm. Res.* **390**, 106703 (2020).

39. Muffler, L. J. P., White, D. E. & Truesdell, A. H. Hydrothermal explosion craters in Yellowstone National Park. *GSA Bull.* **82**, 723–740 (1971).

40. Montanaro, C. et al. Multidisciplinary constraints of hydrothermal explosions based on the 2013 Gengissig Lake events, Kverkfjöll volcano, Iceland. *Earth Planet. Sci. Lett.* **434**, 308–319 (2016).

41. Allahbakhshi, M. et al. Geothermal explosion at the 2014 landslide-covered area of the Geyser Valley, Kamchatka, Russian Far East. *GeoHazards* **4**, 60–76 (2023).

42. Van Vliet-Lanoë, B. et al. Volcanoes and climate: the triggering of preboreal Jökulhlaups in Iceland. *Int. J. Earth Sci.* **109**, 847–876 (2020).

43. Shoemaker, E. S. et al. Mapping ice buried by the 1875 and 1961 Tephra of Askja Volcano, Northern Iceland using ground-penetrating radar: implications for Askja Caldera as a geophysical testbed for in situ resource utilization. *J. Geophys. Res. Planets* **129**, e2023JE007834 (2024).

44. Whalley, W. B. & Azizi, F. Rock glaciers and protalus landforms: Analogous forms and ice sources on Earth and Mars. *J. Geophys. Res. Planets* **108**. https://doi.org/10.1029/2002JE001864 (2003).

45. Fritz, M. et al. Holocene ice-wedge polygon development in northern Yukon permafrost peatlands (Canada). *Quat. Sci. Rev.* **147**, 279–297 (2016).

46. Morino, C. et al. Molards as an indicator of permafrost degradation and landslide processes. *Earth Planet. Sci. Lett.* **516**, 136–147 (2019).

47. Jin, H. et al. Permafrost Degradation and Its Hydrogeological Impacts. *Water*. **14**. https://doi.org/10.3390/w14030372 (2022).

48. Faccenna, C., Florindo, F., Funiciello, R. & Lombardi, S. Tectonic setting and Sinkhole Features: case histories from western Central Italy. *Quat. Proc.* **3**, 47–56 (1993).

49. Jorgenson, M. T. *8.20 Thermokarst Terrains*. (ed. Shroder, J. F. B. T.-T. on G.) 313–324 (Academic Press, 2013).

50. Deline, P. et al. Ice loss from glaciers and permafrost and related slope instability in high-mountain regions. in *Hazards and Disasters Series* (eds Haeberli, W. & Whiteman Risks, and Disasters, (Second Edition), C. B. T.-S. and I.-R. H) Chapter 15, 501–540 (Elsevier, 2021).

51. Dvigalo, V. N. & Melekestsev, I. V. The geological and geomorphic impact of catastrophic landslides in the Geyser Valley of Kamchatka: aerial photogrammetry. *J. Volcanol. Seismol.* **3**, 314–325 (2009).

52. Wolf, P. R., Dewitt, B. A. & Wilkinson, B. E. *Elements of Photogrammetry with Applications in GIS*. (McGraw-Hill Education, 2014).

53. Knuth, F. et al. Historical structure from motion (HSfM): automated processing of historical aerial photographs for long-term topographic change analysis. *Remote Sens. Environ.* **285**, 113379 (2023).

54. Belart, J. M. C. et al. The geodetic mass balance of Eyjafjallajökull ice cap for 1945–2014: processing guidelines and relation to climate. *J. Glaciol.* **65**, 395–409 (2019).

55. Shevchenko, A. V. et al. The rebirth and evolution of Bezymianny volcano, Kamchatka after the 1956 sector collapse. *Commun. Earth Environ.* **1**, 15 (2020).

56. Vivone, G. *Pansharpening. Hyperspectral Imaging* (ed Amigo, J. M. B.) Chapter 2.3, Vol. 32, 69–91 (Elsevier, 2019).

Acknowledgements

Author contributions

A.V.S. collected fieldwork data in 2022 (together with E.U.Z.) and in 2023, processed archive, Plèiades, and partially drone data, performed data analysis and mapping, led the article writing and made all figures; T.R.W. supervised fieldwork 2022 and 2023, participated in data analysis, and contributed to the discussion; M.T.G. provided several ideas and

contributed to the discussion; J.M.C.B. provided archive data and assisted in processing; P.M. collected fieldwork data (together with D.M.) in 2019 and processed the 2019 dataset; E.U.Z. performed processing of the 2022 infrared dataset; Þ.S. and J.K.H contributed to the discussion; J.M.T. and M.S.V. participated in the 2023 fieldwork and together with M.M. and D.M. contributed to the discussion.

Competing interests
All authors declare no competing interests.

Additional information
Supplementary information The online version contains supplementary material available at https://doi.org/10.1038/s43247-024-01616-z.

Correspondence and requests for materials should be addressed to Alina V. Shevchenko.

Peer review information *Communications Earth & Environment* thanks Matthieu Kervyn de Meerendre and Joel Ruch for their contribution to the peer review of this work. Primary Handling Editor: Carolina Ortiz Guerrero. A peer review file is available

Reprints and permissions information is available at http://www.nature.com/reprints

Publisher's note Springer Nature remains neutral with regard to jurisdictional claims in published maps and institutional affiliations.